Journal of Materials Chemistry A

PAPER

View Article Online
View Journal | View Issue

Cite this: J. Mater. Chem. A, 2016, 4, 18516

Ultrafast carrier dynamics in $BiVO_4$ thin film photoanode material: interplay between free carriers, trapped carriers and low-frequency lattice vibrations†

K. T. Butler,[a] B. J. Dringoli,[b] L. Zhou,[cd] P. M. Rao,[cd] A. Walsh[e] and L. V. Titova*[b]

Received 21st August 2016
Accepted 4th November 2016

DOI: 10.1039/c6ta07177e

www.rsc.org/MaterialsA

We explore ultrafast carrier dynamics and interactions of photoexcited carriers with lattice vibrational modes in $BiVO_4$ photoanode material using time-resolved terahertz spectroscopy and first-principles phonon spectrum calculations. We find that photoexcited holes form bound polaron states by introducing lattice distortion that changes phonon spectrum and suppresses the A_g phonon mode associated with opposite motion of Bi and VO_4 molecular units. At excitation fluence higher than 1 mJ cm^{-2} (or 2×10^{15} cm^{-2} per pulse), lattice distortion due to self-localized holes alters the lattice symmetry and vibrational spectrum, resulting in bleaching of THz absorption by A_g phonons. Concurrently, we observe a short lived population of free carriers which exhibit Drude conductivity with mobility on the order of 200 cm^2 V^{-1} s^{-1}, orders of magnitude higher than typical carrier mobility in $BiVO_4$. The anomalously high carrier mobilities are explained in the framework of a Mott transition. This demonstration of enhanced transport suggests how engineering $BiVO_4$ photoanodes to take advantage of free carrier transport under high excitation conditions may in the future significantly enhance performance of photoelectrochemical devices.

Introduction

Due to its moderate bandgap, high photochemical stability, and band edge positions favorable for water oxidation, $BiVO_4$ is considered one of the most promising photoanode metal oxides.[1–4] However, the reported solar-to-hydrogen efficiency of $BiVO_4$ photoanodes is still significantly lower than theoretically predicted values. The major performance bottleneck is poor separation of the photoexcited electron–hole pairs due to the extremely low carrier mobility ($\sim 10^{-2}$ cm^2 V^{-1} s^{-1}), which results in significant carrier recombination losses.[4,5] To an extent, the long (on the order of 50 ns) lifetime of photoexcited carriers compensates for the low mobility; however, identifying possible avenues of increasing mobility would significantly improve $BiVO_4$ photoanode efficiency.[5]

Low charge carrier mobility in $BiVO_4$ is a consequence of strong carrier-phonon coupling, which favors formation of polarons, which are localized carriers (electrons or holes) accompanied by lattice distortion.[6–10] Photoexcited electrons are thought to form small polarons, which are localized on the atomic scale around V^{4+} sites and move by thermally activated hopping, with an estimated activation energy on the order of 0.35 eV.[6,8,11] The resulting electron diffusion length in undoped $BiVO_4$ at room temperature is as low as 10 nm.[12] Transport of photoexcited holes, which is critically important for the performance of the photoanode, is not yet well understood: while some theoretical studies predict small hole polarons with holes localized on O^- sites,[11] others find that large hole polarons that spread over many lattice sites and exhibit band-like transport are more likely to form in the monoclinic form of $BiVO_4$.[7] The hole diffusion length ($\sim$100 nm) in $BiVO_4$ is an order or magnitude larger than that of electrons.[10]

Understanding the dynamics of photoexcited carriers and their coupling to lattice vibrational modes at early times (1–20 ps) after photon absorption is essential for elucidating carrier transport mechanisms in $BiVO_4$ and addressing limitations of $BiVO_4$ photoanodes. Ultrafast carrier dynamics in $BiVO_4$ have been probed using transient optical absorption.[13–16] These studies have indicated that photogenerated holes are trapped with a time constant on the order of 5–15 ps, giving rise to several long-lived absorption bands.[13,14,16] The trapped holes are

[a]Department of Chemistry, University of Bath, BA2 7AY, UK
[b]Department of Physics, Worcester Polytechnic Institute, Worcester, MA, 01609, USA. E-mail: ltitova@wpi.edu
[c]Department of Mechanical Engineering, Worcester Polytechnic Institute, Worcester, MA, 10609, USA
[d]Materials Science and Engineering Graduate Program, Worcester Polytechnic Institute, Worcester, MA 01609, USA
[e]Department of Materials, Imperial College London, SW7 2AZ, UK

† Electronic supplementary information (ESI) available. See DOI: 10.1039/c6ta07177e

coupled to a low energy phonon mode, with irreducible representation A_g, associated with the opposite motion of Bi^{3+} and VO_4^{3-}.[13,14] Coherent excitation of this phonon mode occurs simultaneously with the hole trapping suggesting that hole–lattice interaction favors formation of polarons within a few picoseconds following excitation.

In this study, we explore photoconductive properties of $BiVO_4$ with time-resolved THz spectroscopy (TRTS). A non-contact probe of microscopic conductivity, TRTS has already been successfully applied to uncover ultrafast carrier dynamics and conductivity mechanisms in a variety of bulk and nanostructured materials for solar energy conversion.[17–27] As the bandwidth of THz pulses spans from ~0.2 to 2.4 THz (8–80 cm^{-1}), corresponding to the energy range of 1–10 meV, transmission of THz pulses through samples is intrinsically sensitive to motion of free carriers over length scales of tens of nanometers as well as to low-frequency (<80 cm^{-1}) phonon modes. As a result, TRTS simultaneously provides insights into the dynamics of photoexcited carriers and carrier–lattice interactions that are not accessible by other techniques. Combining THz photoconductivity measurements with first-principles calculations of effects of photoexcitation on lattice dynamics allows us to elucidate the role of carrier-phonon coupling in photoconductivity of $BiVO_4$ photoanodes. We find that at high carrier excitation density, vibrational excitation of the A_g mode by the THz probe pulse is hindered. This happens as a significant number of trapped holes are accompanied by local lattice distortions, and the IR-active A_g mode is transformed into other modes that do not couple to THz probe pulses efficiently. At the same time we observe a short-lived excess of free carriers with mobility which is several orders of magnitude higher than typical carrier mobility in $BiVO_4$.[8–10] Moreover, effective mass theory predicts a Mott transition – whereby a critical density of localised states overlaps to form an extended band-like state – in the region of 10^{16} to 10^{17} cm^{-3}, which can explain the jump in conductivity associated with the bleaching of the A_g phonon mode. We briefly consider how this finding may be exploited to improve $BiVO_4$ device performance through structural engineering.

Methods

Sample preparation

A 1 micron thick $BiVO_4$ film that was drop-cast onto a quartz substrate was used in this study. Clear fused quartz (Quartz Scientific) substrates were sonicated and cleaned 3 times in 1 : 1 : 1 isopropanol alcohol, acetone and DI water mixture. The solution for drop-casting $BiVO_4$ was composed of 0.1225 g $Bi(NO_3)_3 \cdot 5H_2O$ (98%, Sigma Aldrich) and 0.0663 g $OV(C_5H_7O_2)_2$ (98%, Sigma Aldrich), dissolved in 5 mL acetic acid (≥99.7%, Sigma Aldrich) and 0.25 mL acetylacetone (≥99%, Sigma Aldrich) by 30 minutes sonication. The substrate was soaked in acetic acid for 10 minutes and then dried by air-gun, which was found to improve the subsequent wetting and coating of the drop-casting solution. Two drops of 5 μL solution were then dropped onto the substrate, which was then dried on a hotplate set at 500 °C in air for 10 minutes to make one $BiVO_4$ drop-casted layer. After 3 layers of drop-casting, the sample was annealed in a furnace in air at 550 °C for 2 hours to crystallize the $BiVO_4$. An SEM micrograph of the resulting film is shown in ESI Fig. S1.†

Time-resolved THz spectroscopy

Charge carriers in the $BiVO_4$ film were excited by the 400 nm pump pulses generated by frequency doubling of 800 nm, 100 fs pulses from 1 kHz an amplified Ti:sapphire laser (Coherent© Libra HE). Based on a literature value of the absorption coefficient at 400 nm, carriers were phonoinjected into a thin, ~50 nm layer of the $BiVO_4$ film.[28] Photoinduced changes in the sample properties were probed by time-delayed THz pulses generated by optical rectification of 800 nm from the same laser source in a 1 mm thick [110] ZnTe crystal. THz pulses transmitted through the sample were coherently detected by free-space electro-optic sampling in a second [110] ZnTe crystal.

Lattice dynamics calculations

First-principles density functional theory (DFT) calculations were performed using the VASP code within the projector augmented wave formalism.[29,30] The neutral and singly-charged structures were geometry-optimised using the non-local HSE06 exchange-correlation functional.[31] The monoclinic unit cell was expanded to a 2 × 2 × 2 supercell and the *k*-point sampling was carried out using Γ-point only. The phonon spectra were then calculated using a finite displacements approach to form the Hessian of the system. The post-processing and construction of the dynamical matrix and phonon density of states was performed using the PHONOPY package.[32]

Results and discussion

The change in transmission of the main peak of the THz probe pulse ($-\Delta T/T$, Fig. 1) as a function of the delay between the

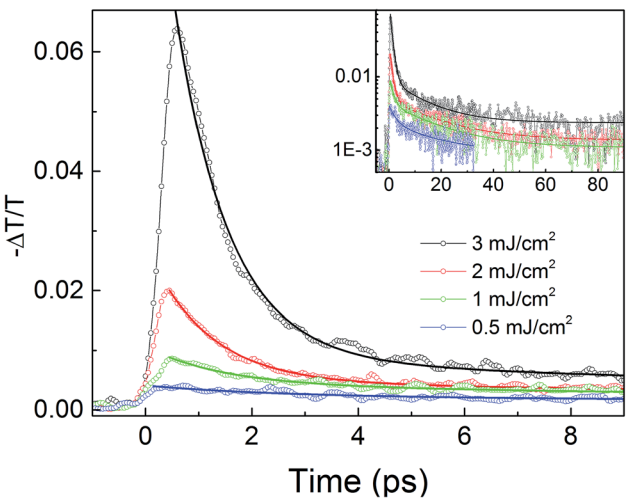

Fig. 1 Change in transmission of the main peak of the THz probe pulse as a function of time delay with respect to a 400 nm, 100 fs pump pulse with fluence from 0.5 to 3.0 mJ cm^{-2}. Solid lines are fits to a double-exponential decay. Inset shows the same data plotted on a semi-logarithmic scale in a larger delay time range.

pump pulse and THz probe pulse is proportional to the time-dependent photoconductivity.[19] The photoconductivity exhibits a bi-exponential decay with a small offset that is constant over the experimental time range (<120 ps), and solid lines in Fig. 1 represent fits of the experimental data to a bi-exponential decay function $-\frac{\Delta T}{T} = A_1 \exp\left(-\frac{t}{t_1}\right) + A_2 \exp\left(-\frac{t}{t_2}\right) + \text{const.}$ The amplitude A_1 and to a lesser extent, the decay time t_1 of the fast component, strongly depend on the photoexcitation conditions. Barely present for 0.5 mJ cm^{-2} excitation fluence, the fast decay contribution represented by A_1 increased nearly 60-fold for 3.0 mJ cm^{-2} fluence. The decay time t_1 of the fast component decreased from 2.3 ± 0.6 ps for the lowest fluence to 1.0 ± 0.1 ps for the highest fluence. The decay time of the slower component is independent of fluence at 16.5 ± 2.5 ps, and its contribution to overall photoconductivity dynamics scales linearly with excitation. Finally, the small constant offset likely varies on the time scale of tens of nanoseconds, as seen in time-resolved microwave conductivity measurements of a similar $BiVO_4$ film.[13]

Elucidating the nature of the processes that give rise to the observed fast photoconductivity dynamics requires analysis of the complex-valued, frequency-dependent THz conductivity spectra as a function of pump-probe delay times and excitation fluence. Frequency-dependent changes in sample properties induced by the pump pulse can be determined by detecting the changes in the amplitude and phase of the transmitted THz pulse. Fig. 2(a) shows the THz pulse transmitted through the unexcited $BiVO_4$ film and the change in THz waveform 2 ps following excitation with a 3.0 mJ cm^{-3} fluence. Corresponding frequency-resolved transmitted THz intensities (proportional to the square of the amplitude) without photoexcitation and 2 ps after photoexcitation are given in Fig. 2(b). Photoexcitation slightly increases absorption of lower THz frequencies (<1.5 THz), and enhances transmission in ~1.5–2.2 THz range. While those changes are subtle, they are clearly visible in the photo-induced absorbance change, Fig. 2(c) and conductivity, Fig. 2(d). The photoinduced THz absorption at low frequencies, which we will discuss shortly, can be attributed to free carrier absorption. The photoinduced reduction of THz absorption at higher frequencies can be fitted to a Lorentzian peak centered at $\omega_{A_g}/2\pi = 1.92$ THz (or 64 cm^{-1}) with the damping constant $\Gamma_{A_g}/2\pi = 0.48$ THz (Fig. 2(c)). The center frequency of this absorption bleach feature is close to the frequency of the A_g phonon mode, which earlier transient optical absorption studies found to be coherently excited by 400 nm pulses.[13,14] The total photo-induced change in conductivity (Fig. 2(d)) can be expressed as a combination of the Drude free carrier component and suppression of the Lorentz oscillator that represents the A_g phonon,

$$\hat{\sigma}(\omega) = \hat{\sigma}_{\text{Drude}}(\omega) - \hat{\sigma}_{\text{Lorentz}}(\omega) = \frac{Ne^2\tau}{m^*(1 - i\omega\tau)} - \frac{\varepsilon_0 S_{A_g}\omega}{\left(\omega_{A_g}{}^2 - \omega^2\right)^2 + \left(\Gamma_{A_g}\omega\right)^2} \times \left(\Gamma_{A_g}\omega - i\left(\omega_{A_g}{}^2 - \omega^2\right)\right). \quad (1)$$

Here, N is the free charge carrier density averaged over the volume sampled by the THz pulse, m^* is the carrier effective mass, τ is the Drude carrier scattering time, S_{A_g} is the oscillator strength of the A_g phonon, ω is the frequency, and ε_0 is the vacuum permittivity.

Fig. 3 summarizes the effects of excitation fluence on photoconductivity by following the THz absorption bleach as well as the frequency-resolved complex photoconductivity detected 2 ps after photoexcitation. Most notably, the absorption bleach in the vicinity of the A_g phonon mode becomes significantly more pronounced with increasing excitation fluence (Fig. 3(a)). At the same time, complex conductivity at low frequencies (<1.5 THz) acquires Drude-like character, indicating the presence of free carriers at early times after excitation (Fig. 3(b)). In the following discussion we analyze the photoinduced conductivity changes in this low frequency range that are not significantly affected by the absorption bleach at 1.92 THz within the framework of the Drude model. Lines in Fig. 3(b) are simultaneous fits of real (solid red squares) and imaginary (open blue circles) THz conductivity to the Drude model, $\hat{\sigma}_{\text{Drude}}(\omega) = \frac{Ne^2\tau}{m^*(1 - i\omega\tau)}$.

Taking a band effective mass for both electrons and holes as $0.3m_e$ from previous calculations[33] and from the band structures calculated in this study, fitting complex conductivity to the Drude model yields instantaneous carrier density N as well as the carrier relaxation time τ. The relaxation time, 35 fs ± 10 fs, is

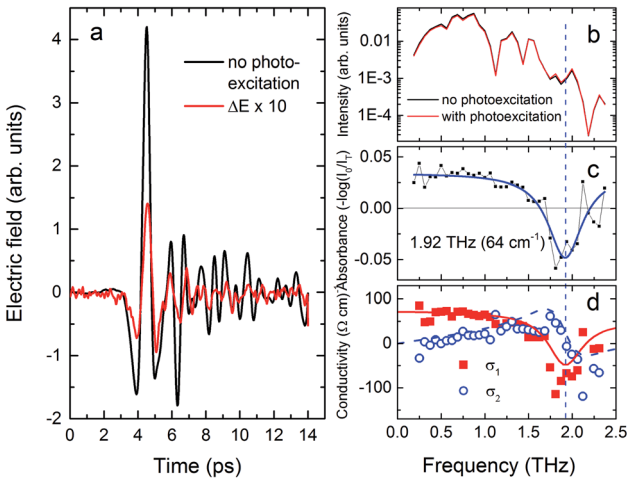

Fig. 2 Effects of photoexcitation with 3.0 mJ cm^{-2}, 400 nm pulse at pump-probe delay of 2 ps. (a) THz waveform, transmitted through $BiVO_4$ film without photoexcitation, and the change in the waveform due to excitation (scaled by a factor of 10 for clarity). (b) THz intensity (proportional to the square of the electric field amplitude) transmitted through non-excited and photoexcited sample, and (c) the corresponding photoinduced chance in THz absorbance (c) and complex conductivity (d). Solid line in (c) shows the fit of the experimental transient THz absorbance to a Lorentz function with the center frequency $\omega_{A_g}/2\pi = 1.92$ THz and the damping constant $\Gamma_{A_g}/2\pi = 0.48$ THz. Solid and dashed lines in (d) a fit of the photoinduced real conductivity σ_1 (solid red line) and imaginary conductivity σ_2 (dashed blue line) to a Drude–Lorentz conductivity (eqn (1)) with $\tau = 35$ fs and $N = 2 \times 10^{18}$ cm^{-3}.

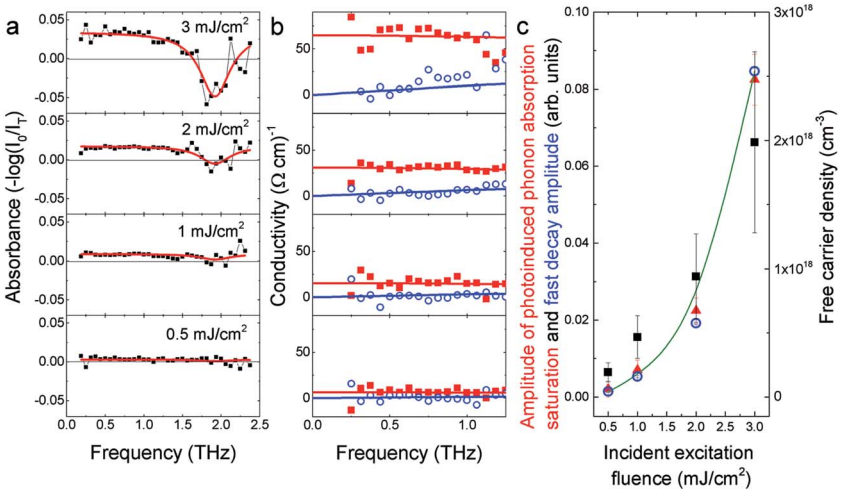

Fig. 3 Excitation fluence dependence of photoinduced conductivity and phonon absorption bleach as observed 2 ps after photoexcitation. (a) Absorbance spectra at fluence ranging from 0.5 to 3.0 mJ cm^{-2}, (b) corresponding complex conductivity spectra, with red squares indicating real, and blue circles – imaginary conductivity components, and the lines representing fitting of data to the Drude conductivity model. (c) Fluence dependence of amplitude of photoinduced absorption bleach (red triangles), fast component of photoconductivity decay A_1 (Fig. 1) (blue circles), and free photoexcited carrier density determined from Drude fit to frequency-resolved conductivity (black squares) (b). The green solid line is a guide to the eye.

found to be independent of excitation fluence or time after excitation, and the corresponding mobility $\mu = e\tau/m^*$ of short-lived free carrier population excited by 100 fs, 400 nm pulses is ~200 $cm^2\ V^{-1}\ s^{-1}$, several orders of magnitude larger than steady-state carrier mobility associated with thermally-activated polaron transport. Free carrier density N at 2 ps after photoexcitation is plotted in Fig. 3(c) as solid black squares, along with the amplitude of 1.92 THz absorption bleach (solid red triangles) and the amplitude of the fast component of transient conductivity decay ($-\Delta T/T$), shown as open blue circles. This shows that the increase in concentration of free carriers is concurrent with the THz absorption bleach.

Fig. 4 examines time evolution of the observed A_g phonon absorption bleach Fig. 4(a) as well as of free carrier conductivity (Fig. 4(b)) at the highest excitation fluence, 3 mJ cm^{-2}. As the absorption bleach is recovered, Drude-like conductivity decreases. In fact, the amplitude of the absorption bleach and free carrier density both decay on ~1 ps time scale, the same time scale as photoconductivity decay at the same excitation fluence shown in Fig. 1, again suggesting that saturation of phonon absorption under high photoexcitation conditions and existence of free carriers exhibiting band-like transport are related phenomena.

In order to probe the microscopic origins of the photoinduced bleaching in the absorption spectrum we have performed first-principles lattice dynamics calculations. These calculations allow us to investigate how the vibrational spectrum of the crystal structure is affected by the presence of photogenerated carriers. Initially the neutral crystal in the monoclinic structure was fully relaxed and the vibrational spectrum calculated. The eigen frequencies of the Γ-point phonon modes, are plotted in Fig. 5, where the mode experimentally observed at 64 cm^{-1} is highlighted in yellow. It is the A_g mode involving the counter-motion of the Bi^{3+} ions and the VO_4^{3-} units. As this mode involves motion of oppositely charged molecular units, it is expected to be a particularly strong absorber in the infrared. This mode is also depicted by the phonon eigenvectors in the picture below the plot, where the phonon modes are represented by arrows. To simulate the generation of a hole, we then removed an electron from a 2 × 2 × 2 supercell of monoclinic $BiVO_4$. Within the Ewald summation employed, this is neutralised by a uniform negative background charge, thus ensuring charge neutrality and a convergent electrostatic potential. The resultant structure was then optimised, introducing an initial small distortion to allow for the formation of polaron. In this case the electronically perturbed crystal relaxes into a different space group from the neutral structure; $P\bar{4}$, as opposed to $I4_1/a$. The resultant vibrational phonon spectrum is plotted in Fig. 5 (center-right panel). The A_g mode involving the counter-motion of Bi^{3+} ions and the VO_4^{3-} units is no longer present in the phonon spectrum of the crystal with the trapped hole. The removal of the A_g mode from the phonon spectrum in the presence of the excess hole explains the observed photobleaching of this mode with increased photocarrier generation.

Under high excitation levels, the resulting transient temperature increase may lead to the increase in hopping mobility. However, the hopping mobility in an ideal oxide semiconductor has been demonstrated to have an upper limit of ~70 $cm^2\ V^{-1}\ s^{-1}$,[34] significantly lower that the mobility observed in our measurements. Instead, we propose that the concurrent observation of suppression of absorption by the A_g mode and enhanced carrier transport may be related to a Mott transition. Above a certain critical concentration, localised charge carriers begin to interact and band-like transport is observed. The phenomenon of insulator to metallic conduction as a result of condensation of lattice impurities was described

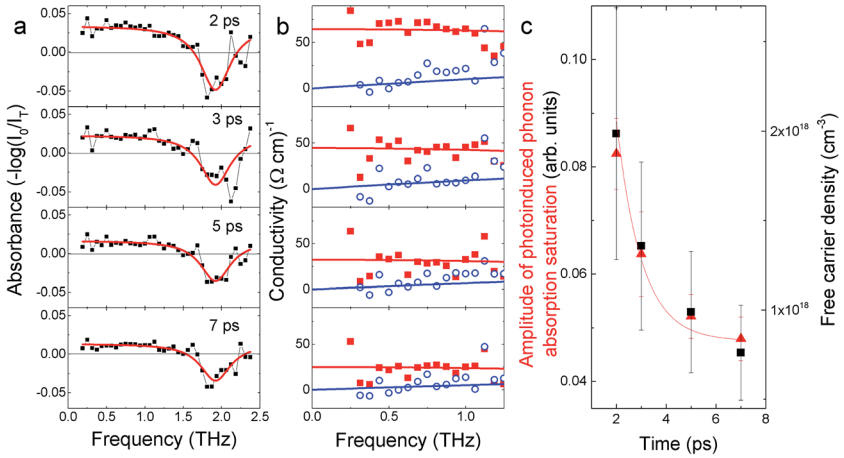

Fig. 4 Time dependence of photoinduced conductivity and phonon absorption bleach observed after photoexcitation with 3.0 mJ cm^{-2} fluence. (a) Absorbance spectra at pump-probe delay times from 2 ps to 7 ps, (b) corresponding complex conductivity spectra, with red squares indicating real, and blue circles – imaginary conductivity components, and the lines representing fitting of data to the Drude conductivity model. (c) Time dependence of the amplitude of the photoinduced absorption bleach (red triangles), and free photoexcited carrier density determined from a Drude fit to the frequency-resolved conductivity (b). The red line is a single exponential decay curve with 1 ps decay time, used as a guide to the eye.

by Mott as the metal-nonmental (MNM) transition, originally in the context of dopants in group-IV semiconductors.[35] Edwards and Sienko subsequently demonstrated the wider applicability of Mott criterion.[36] In the case of $BiVO_4$ a critical concentration of self-trapped holes, which cause the photo bleaching, can be related to the high carrier mobility.

In a semiconductor matrix an isolated electronic defect (in our case the trapped hole) can be associated with a characteristic Bohr radius, which in turn is determined by the effective mass of the hole and the dielectric constant of the matrix; from effective mass theory,[37] $r_b = \frac{\varepsilon_{st}}{m_h^*}$, where ε_{st} is the static dielectric constant, previously calculated as 52 (ref. 38) and m_h^* is the hole effective mass, which is calculated from the band structure to be $0.3m_e$, in agreement with previous calculations.[33,38] At a critical concentration of these impurity wavefunctions overlap in the matrix to form a continual band. At this concentration the carriers in the impurity (hole) band can travel freely throughout the material, resulting in metallic conduction. The concentration (c) is obtained from $c = \frac{1}{4/3\pi {r_b}^3}$.

Taking values for the physical properties discussed above, we obtain a critical concentration for the MNM transition of the order of 2×10^{16} cm^{-3}. This is below the value of the measured free carrier concentration $\sim 10^{17}$ cm^{-3} and suggests that the observed free carrier transport can arise as a result of the coalescence of localised states to form a transport band above a critical concentration. This critical concentration is only accessed when the intensity of incident radiation is sufficiently high to generate enough trapped holes. At these high fluences, saturation of the polaron hole states and the corresponding absorption bleach saturation occur very quickly, on sub-ps time scales after excitation, as has been suggested in earlier transient optical absorption studies.[13,14] With fluence above the critical threshold of ~ 1 mJ cm^{-2}, a significant portion of the polaron trap states are filled within a very short time, and an increase in fluence results in significant increase in free carrier concentration as manifested by the superlinear increase in the peak photoconductivity (Fig. 1). As self-trapped holes recombine with either free or trapped electrons and their concentration falls below the Mott concentration, band-like transport of the remaining photoexcited carriers is suppressed. At the same time, THz absorption by the A_g mode recovers. This occurs over 1–2 ps time scales. The experimentally-determined onset of the THz absorption bleach and concurrent band-like transport occurs when photoinjected carrier density is on the order of 10^{20} cm^{-3}. This is significantly higher than the estimated Mott concentration and the measured free carrier density values, indicating that most photoinjected carriers in high excitation regime are lost to recombination over ultra-short, sub-picosecond time scales that are not accessible in our experiments.

The observation of free carriers offers the possibility that the low conductivity bottleneck for the application of $BiVO_4$ as a photoelectrode may be surmounted under constant concentrated illumination. The rapid recombination and decay of the carriers means that careful device structuring is required to exploit the improved conductivity. We can estimate the carrier diffusion length (L_{Diff}) of the band-like carriers from $L_{Diff} = \sqrt{\frac{k_B T}{e}\mu t}$, where T is the temperature, e is the elementary charge and the mobility and t is the carrier lifetime from generation until recombination, extraction or trapping.[39] Taking t as ~ 1 ps, which is the lifetime of free carriers in the high excitation fluence regime (Fig. 4(c)) and $\mu = 200$ cm^2 V^{-1} s^{-1}, we obtain a characteristic diffusion length of 22 nm. This means that engineering of nanostructured $BiVO_4$, with greater surface to volume ratios, in

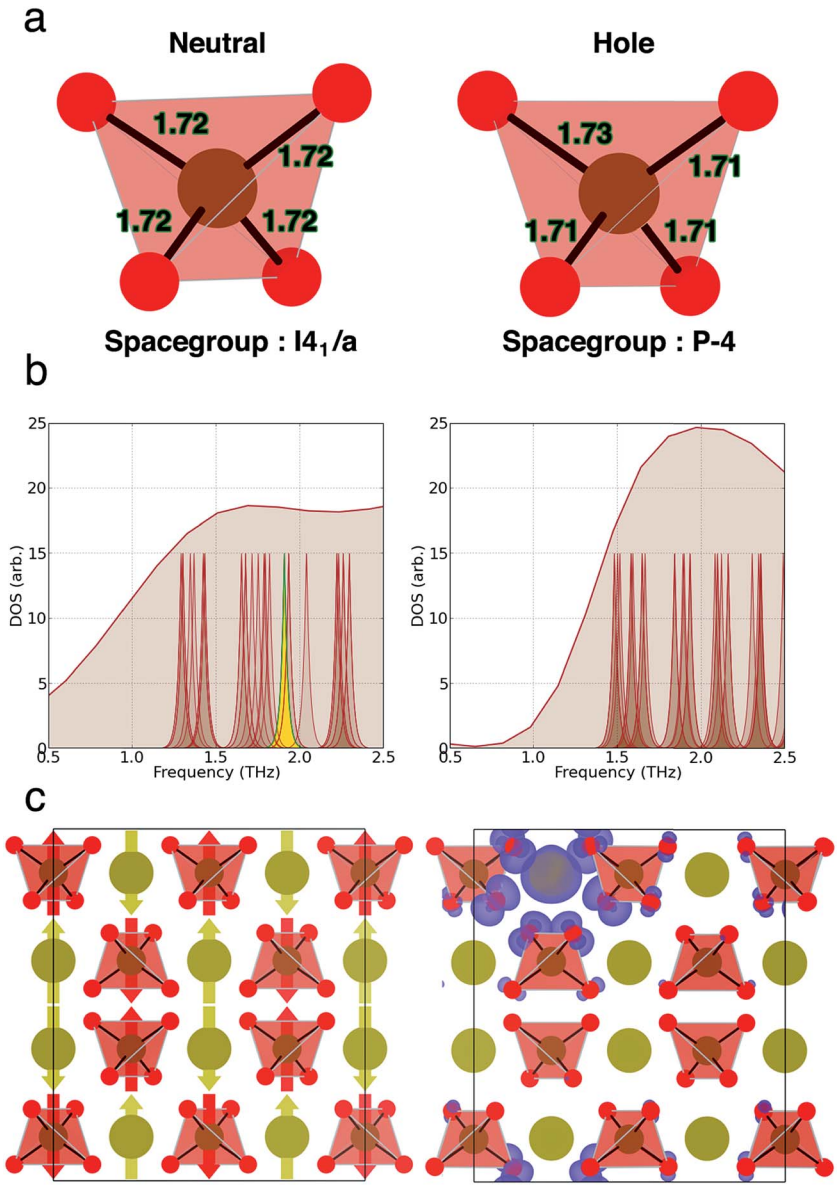

Fig. 5 Results from density functional theory calculations of $BiVO_4$; left charge neutral; right with a hole. (a) VO_4 tetrahedral geometries showing the effects of polaron formation on the local bond lengths around a V site. (b) Vibrational phonon peaks at the Γ-point, with full phonon density of states (DOS) in the background. (c) Left, the A_g phonon mode in the neutral species; Right, real-space localisation of the hole in the charged crystals, with hole density (blue isosurface) spread over a Bi site and the neighbouring O atoms.

association with optical concentration to achieve enhanced fluence could result in photoanodes with all of the desirable properties of bulk $BiVO_4$, but greatly improved carrier mobilities. Possible avenues for realizing this regime may involve the use of nano-plasmonic devices to significantly concentrate light in nanostructured $BiVO_4$. However, care must be taken to avoid thermally damaging the material, if continuous excitation is to be used. Future studies will determine the photodamage thresholds in nano-plasmonic and $BiVO_4$ composites.

In conclusion, we have studied photoexcited carrier dynamics in $BiVO_4$ photoanode material using time-resolved terahertz spectroscopy. Extremely low carrier mobility due to pronounced polaron effects is known to limit efficiency of $BiVO_4$ photoanodes. We find that above a threshold excitation density of 10^{15} photons per cm^2 per 400 nm pulse, polaron states population surpasses critical Mott concentration, and a short-lived excess free carriers exhibit band-like transport with mobility on the order of 200 $cm^2\ V^{-1}\ s^{-1}$. Furthermore, combining terahertz spectroscopy with lattice dynamics calculations, we have shown that photoexcited holes form bound polaron states by introducing lattice distortion that alters changes the lattice symmetry and suppresses absorption at 1.92 THz (64 cm^{-1}) by A_g phonon mode. These findings will be important for engineering efficient nanostructured $BiVO_4$ photoanodes.

Acknowledgements

This material is based upon work supported by the National Science Foundation under Grant No. DMR-1609538. P. M. R. and L. V. T. acknowledge start-up funding by Worcester Polytechnic Institute. K. T. B. and A. W. acknowledge membership of the UK's HPC Materials Chemistry Consortium (EPSRC EP/L000202) and access to computational resources through PRACE. A. W. acknowledges support from the Royal Society for a University Research Fellowship and K. T. B. is funded by EPSRC (EP/M009580/1 and EP/J017361/1). Finally, B. J. D. is grateful for Summer Undergraduate Research Fellowship by Worcester Polytechnic Institute.

References

1 F. F. Abdi, L. Han, A. H. M. Smets, M. Zeman, B. Dam and R. van de Krol, Efficient solar water splitting by enhanced charge separation in a bismuth vanadate-silicon tandem photoelectrode, *Nat. Commun.*, 2013, **4**, 2195.

2 L. Zhou, C. Zhao, B. Giri, P. Allen, X. Xu, H. Joshi, L. V. Titova and P. M. Rao, High Light Absorption and Charge Separation Efficiency at Low Applied Voltage from Sb-Doped SnO_2/$BiVO_4$ Core/Shell Nanorod-Array Photoanodes, *Nano Lett.*, 2016, **16**(6), 3463–3474.

3 J. Yu and A. Kudo, Effects of Structural Variation on the Photocatalytic Performance of Hydrothermally Synthesized $BiVO_4$, *Adv. Funct. Mater.*, 2006, **16**(16), 2163–2169.

4 T. W. Kim and K.-S. Choi, Nanoporous $BiVO_4$ Photoanodes with Dual-Layer Oxygen Evolution Catalysts for Solar Water Splitting, *Science*, 2014, **343**(6174), 990–994.

5 F. F. Abdi, T. J. Savenije, M. M. May, B. Dam and R. van de Krol, The Origin of Slow Carrier Transport in $BiVO_4$ Thin Film Photoanodes: A Time-Resolved Microwave Conductivity Study, *J. Phys. Chem. Lett.*, 2013, **4**(16), 2752–2757.

6 K. E. Kweon, G. S. Hwang, J. Kim, S. Kim and S. Kim, Electron small polarons and their transport in bismuth vanadate: a first principles study, *Phys. Chem. Chem. Phys.*, 2015, **17**(1), 256–260.

7 K. E. Kweon and G. S. Hwang, Structural phase-dependent hole localization and transport in bismuth vanadate, *Phys. Rev. B: Condens. Matter Mater. Phys.*, 2013, **87**(20), 205202.

8 A. J. E. Rettie, W. D. Chemelewski, J. Lindemuth, J. S. McCloy, L. G. Marshall, J. S. Zhou, *et al.* Anisotropic small-polaron hopping in W: $BiVO_4$ single crystals, *Appl. Phys. Lett.*, 2015, **106**(2), 022106.

9 A. J. Rettie, W. D. Chemelewski, D. Emin and C. B. Mullins, Unravelling Small-Polaron Transport in Metal Oxide Photoelectrodes, *J. Phys. Chem. Lett.*, 2016, **7**(3), 471–479.

10 A. J. E. Rettie, H. C. Lee, L. G. Marshall, J.-F. Lin, C. Capan, J. Lindemuth, *et al.* Combined Charge Carrier Transport and Photoelectrochemical Characterization of $BiVO_4$ Single Crystals: Intrinsic Behavior of a Complex Metal Oxide, *J. Am. Chem. Soc.*, 2013, **135**(30), 11389–11396.

11 T. Liu, X. Zhou, M. Dupuis and C. Li, The nature of photogenerated charge separation among different crystal facets of $BiVO_4$ studied by density functional theory, *Phys. Chem. Chem. Phys.*, 2015, **17**(36), 23503–23510.

12 J. A. Seabold, K. Zhu and N. R. Neale, Efficient solar photoelectrolysis by nanoporous Mo:$BiVO_4$ through controlled electron transport, *Phys. Chem. Chem. Phys.*, 2014, **16**(3), 1121–1131.

13 J. Ravensbergen, F. F. Abdi, J. H. van Santen, R. N. Frese, B. Dam, R. van de Krol, *et al.* Unraveling the Carrier Dynamics of $BiVO_4$: A Femtosecond to Microsecond Transient Absorption Study, *J. Phys. Chem. C*, 2014, **118**(48), 27793–27800.

14 N. Aiga, Q. Jia, K. Watanabe, A. Kudo, T. Sugimoto and Y. Matsumoto, Electron–Phonon Coupling Dynamics at Oxygen Evolution Sites of Visible-Light-Driven Photocatalyst: Bismuth Vanadate, *J. Phys. Chem. C*, 2013, **117**(19), 9881–9886.

15 B. Pattengale, J. Ludwig and J. Huang, Atomic Insight into the W-Doping Effect on Carrier Dynamics and Photoelectrochemical Properties of $BiVO_4$ Photoanodes, *J. Phys. Chem. C*, 2016, **120**(3), 1421–1427.

16 I. Grigioni, K. G. Stamplecoskie, E. Selli and P. V. Kamat, Dynamics of Photogenerated Charge Carriers in WO_3/$BiVO_4$ Heterojunction Photoanodes, *J. Phys. Chem. C*, 2015, **119**(36), 20792–20800.

17 J. B. Baxter, C. Richter and C. A. Schmuttenmaer, Ultrafast Carrier Dynamics in Nanostructures for Solar Fuels, *Annu. Rev. Phys. Chem.*, 2014, **65**, 423–447.

18 R. L. Milot and C. A. Schmuttenmaer, Electron Injection Dynamics in High-Potential Porphyrin Photoanodes, *Acc. Chem. Res.*, 2015, **48**(5), 1423–1431.

19 L. V. Titova, T. L. Cocker, D. G. Cooke, X. Wang, A. Meldrum and F. A. Hegmann, Ultrafast percolative transport dynamics in silicon nanocrystal films, *Phys. Rev. B: Condens. Matter Mater. Phys.*, 2011, **83**(8), 085403.

20 P. Parkinson, J. Lloyd-Hughes, M. B. Johnston and L. M. Herz, Efficient generation of charges *via* below-gap photoexcitation of polymer-fullerene blend films investigated by terahertz spectroscopy, *Phys. Rev. B: Condens. Matter Mater. Phys.*, 2008, **78**(11), 115321.

21 P. U. Jepsen, D. G. Cooke and M. Koch, Terahertz spectroscopy and imaging – modern techniques and applications, *Laser Photonics Rev.*, 2011, **5**(1), 124–166.

22 H. Němec, P. Kužel and V. Sundström, Charge transport in nanostructured materials for solar energy conversion studied by time-resolved terahertz spectroscopy, *J. Photochem. Photobiol., A*, 2010, **215**(2–3), 123–139.

23 D. G. Cooke, F. C. Krebs and P. U. Jepsen, Direct Observation of Sub-100 fs Mobile Charge Generation in a Polymer-Fullerene Film, *Phys. Rev. Lett.*, 2012, **108**(5), 056603.

24 G. W. Guglietta, B. T. Diroll, E. A. Gaulding, J. L. Fordham, S. Li, C. B. Murray, *et al.* Lifetime, Mobility, and Diffusion of Photoexcited Carriers in Ligand-Exchanged Lead Selenide Nanocrystal Films Measured by Time-Resolved Terahertz Spectroscopy, *ACS Nano*, 2015, **9**(2), 1820–1828.

25 M. R. Bergren, B. J. Simonds, B. Yan, G. Yue, R. Ahrenkiel, T. E. Furtak, *et al.* Electron transfer in hydrogenated nanocrystalline silicon observed by time-resolved terahertz

spectroscopy, *Phys. Rev. B: Condens. Matter Mater. Phys.*, 2013, **87**(8), 081301.

26 R. Ulbricht, E. Hendry, J. Shan, T. F. Heinz and M. Bonn, Carrier dynamics in semiconductors studied with time-resolved terahertz spectroscopy, *Rev. Mod. Phys.*, 2011, **83**(2), 543–586.

27 C. S. Ponseca Jr, T. J. Savenije, M. Abdellah, K. Zheng, A. Yartsev, T. Pascher, *et al.* Organometal halide perovskite solar cell materials rationalized: ultrafast charge generation, high and microsecond-long balanced mobilities, and slow recombination, *J. Am. Chem. Soc.*, 2014, **136**(14), 5189–5192.

28 J. K. Cooper, S. Gul, F. M. Toma, L. Chen, Y.-S. Liu, J. Guo, *et al.* Indirect Bandgap and Optical Properties of Monoclinic Bismuth Vanadate, *J. Phys. Chem. C*, 2015, **119**(6), 2969–2974.

29 G. Kresse and J. Hafner, *Ab initio* molecular dynamics for liquid metals, *Phys. Rev. B: Condens. Matter Mater. Phys.*, 1993, **47**(1), 558–561.

30 P. E. Blöchl, Projector augmented-wave method, *Phys. Rev. B: Condens. Matter Mater. Phys.*, 1994, **50**(24), 17953–17979.

31 A. V. Krukau, O. A. Vydrov, A. F. Izmaylov and G. E. Scuseria, Influence of the exchange screening parameter on the performance of screened hybrid functionals, *J. Chem. Phys.*, 2006, **125**(22), 224106.

32 A. Togo and I. Tanaka, First principles phonon calculations in materials science, *Scr. Mater.*, 2015, **108**, 1–5.

33 A. Walsh, Y. Yan, M. N. Huda, M. M. Al-Jassim and S. H. Wei, Band Edge Electronic Structure of $BiVO_4$: Elucidating the Role of the Bi s and V d Orbitals, *Chem. Mater.*, 2009, **21**(3), 547–551.

34 K. A. Stewart and J. F. Wager, Thin-film transistor mobility limits considerations, *J. Soc. Inf. Disp.*, 2016, **24**(6), 386–393.

35 N. F. Mott, On the transition tometallic conduction in semiconductors, *Can. J. Phys.*, 1956, **34**(12A), 1356–1368.

36 P. P. Edwards and M. J. Sienko, Universality aspects of the metal-nonmetal transition in condensed media, *Phys. Rev. B: Condens. Matter Mater. Phys.*, 1978, **17**(6), 2575–2581.

37 J. M. Luttinger and W. Kohn, Motion of Electrons and Holes in Perturbed Periodic Fields, *Phys. Rev.*, 1955, **97**(4), 869–883.

38 T. W. Kim, Y. Ping, G. A. Galli and K.-S. Choi, Simultaneous enhancements in photon absorption and charge transport of bismuth vanadate photoanodes for solar water splitting, *Nat. Commun.*, 2015, **6**, 8769.

39 G. Hodes and P. V. Kamat, Understanding the Implication of Carrier Diffusion Length in Photovoltaic Cells, *J. Phys. Chem. Lett.*, 2015, **6**(20), 4090–4092.